Different mechanisms for the seasonal variations of the mesoscale eddy energy in the South China Sea

Yuhui Zhao [a,b], Yang Yang [a,b], X. San Liang [b,c,*], Yuanzhi Zhang [a]

[a] School of Marine Sciences, Nanjing University of Information Science and Technology, Nanjing, China
[b] Center for Ocean-Atmosphere Dynamical Studies, Nanjing University of Information Science and Technology, Nanjing, China
[c] Department of Atmospheric and Oceanic Sciences, Fudan University, Shanghai, China

A B S T R A C T

Using a recently developed functional analysis tool, Multiscale Window Transform (MWT) and the MWT-based theory of canonical transfer, this study investigates the dynamical processes responsible for the seasonal variability of the mesoscale eddies in the South China Sea (SCS). A three-scale energetics framework is employed, in which the original fields are decomposed into subfields on a nonstationary background flow window, a mesoscale eddy window and a high-frequency synoptic eddy window. Three local regions of high mesoscale eddy kinetic energy (EKE) levels, namely, the southwest of Taiwan Island (SWT), the southeast of Vietnam (SEV) and the northeast of the Natuna Island (NEN), are identified. The seasonal cycles of the mesoscale EKE in the three regions are not in phase, with peaks occurring around January, October and December, respectively. By diagnosing the canonical transfers between the background flow and the mesoscale eddies, we find that the seasonal cycle of the eddy variability in the SWT region is due to a mixed instability (baroclinic and barotropic instabilities), while barotropic instability plays a dominant role in determining the EKE seasonality in the SEV and NEN regions. This is quite different from the previous argument that baroclinic instability dominates the seasonal EKE in the SCS. The three-scale framework further reveals that high-frequency synoptic motions act to dissipate the lower-frequency mesoscale eddies through forward energy cascades. Besides the internal processes, external wind forcing is also found to influence the seasonal eddy variability, but is only limited to the NEN region. Our results highlight different mechanisms controlling the seasonal modulations of the mesoscale eddies in different regions of the SCS.

1. Introduction

Mesoscale eddies are ubiquitous in the South China Sea (SCS). Previous studies based on satellite observations have demonstrated that the activities of mesoscale eddies are particularly strong in the northeastern SCS and in the region offshore of Vietnam where strong background flows exist (Hwang and Chen 2000; Wang et al., 2003; Xie et al., 2018). Specifically, in the northeastern SCS, the Kuroshio intrusion through the Luzon Strait into the SCS is observed to occur all year round, with increased intensity in winter (Xue et al., 2004; Nan et al., 2015). As indicated by the arrows in Fig. 1a–b, a major part of the intruded Kuroshio develops into a loop southwest of Taiwan Island, flowing out through the northern Luzon Strait, and the rest part forms a branch further extending into the interior SCS. As for the region off Vietnam, a coastal jet usually called the SCS western boundary current (SCSWBC) occurs mainly in winter and summer

(e.g., Hu et al., 2000; Wang et al., 2013). A salient feature of the SCSWBC distinct from the typical western boundary currents in open oceans is the seasonal reversal of flow direction due to the East Asian monsoon (e.g., Wyrtki 1961; Yang et al., 2002). Following the northeasterly monsoon, the mainstream SCSWBC in winter flows southwestward along the western slope and turns east on approaching the southern boundary (Fig. 1a). In summer, the SCSWBC reverses its direction and becomes a northeastward jet (Fig. 1b) when the southwesterly wind prevails. Intriguingly, when the summer SCSWBC arrives at the east coast of Vietnam, an offshore jet, namely, the Summertime Vietnam Offshore Current (SVOC), often separates from the mainstream at about $11°N$ and continues to flow eastward/northeastward (Cai et al., 2007; Gan and Qu 2008). A cyclonic eddy and an anticyclonic eddy often appear simultaneously on each side of the SVOC, forming a dipole pattern in this region (Wang et al., 2006; Chen et al., 2010).
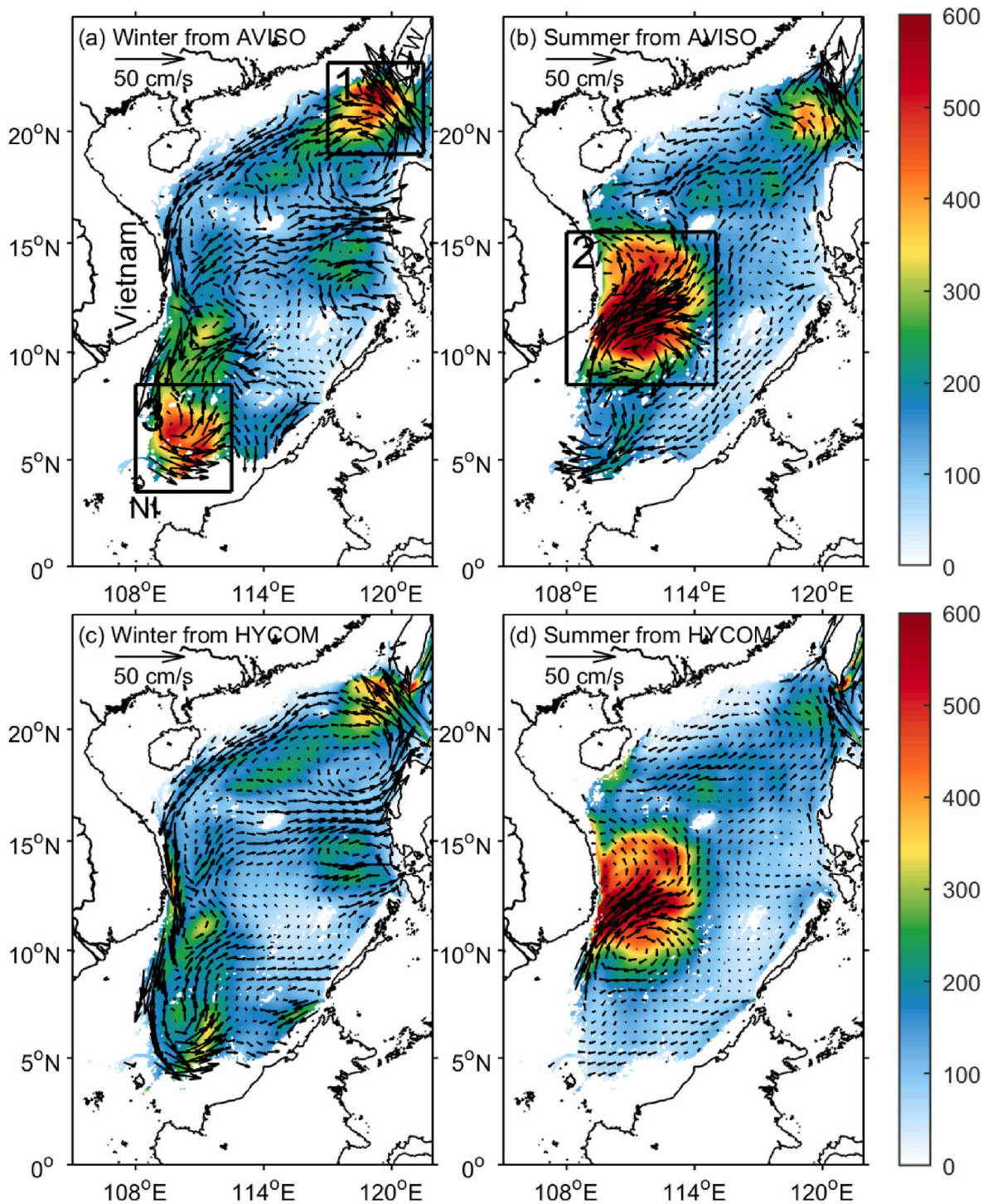
Fig. 1. Long-term mean maps of currents (arrows; cm/s) and mesoscale EKE (shadings; cm^2/s^2) at the surface in winter (left column) and summer (right column) based on AVISO (upper row) and HYCOM (lower row) datasets. Areas shallower than 100 m and adjacent seas are masked to highlight the SCS. "TW" and "NI" in (a) denote Taiwan Island and the Natuna Island, respectively. The boxes in black bold lines marked by 1, 2 and 3 frame the centers of high mesoscale EKE [referred to in the text as SWT (117°-121.5°E, 19°-23°N), SEV (108°-115°E, 8.5°-15.5°N) and NEN (108°-112.5°E, 3.5°-8.5°N), respectively].

Fig. 1a and b shows the long-term mean distributions of the surface mesoscale eddy kinetic energy (EKE) estimated from satellite observation over the SCS in winter and summer, respectively. Areas shallower than 100 m and adjacent seas including the Sulu Sea and the Celebes Sea are masked hereinafter to highlight the SCS. Three centers of high mesoscale eddy variability can be seen from Fig. 1, which are located in the southwest of Taiwan Island (SWT; around 117°-121.5°E and 19°-23°N), the southeast of Vietnam (SEV; around 108°-115°E and 8.5°-15.5°N) and the northeast of the Natuna Island (NEN; around 108°-112.5°E and 3.5°-

8.5°N), respectively (denoted by the black boxes in Fig. 1a–b). Previous studies based on satellite altimetry records reported that the mesoscale EKEs in the first two centers, namely the SWT and SEV regions, have distinct seasonal variations; the former peaks in winter and the latter peaks in fall (e.g., Cheng and Qi 2010; Wang et al., 2012). In contrast, less attention has been paid to the mesoscale eddies in the NEN region. As shown in Fig. 1a and b, the mesoscale EKE in this region exhibits a notable seasonality, which is strong in winter and weak in summer.

Baroclinic instability of the background flow is usually believed to

account for the EKE seasonality in the SCS. For instance, Chen et al. (2012) and Wang et al. (2012) examined the linear growth rate and suggested that baroclinic instability controls the seasonal eddy variability in the SWT and SEV regions. These authors found that the vertical velocity shear of the background flow (as the indicator of baroclinic instability according to linear stability analysis) in the SWT region reaches its maximum in winter, leading to the local maximum of the mesoscale eddy activity in the same season. Although as suggested in these studies baroclinic instability plays an important role in the seasonal modulations of EKE in the SCS, barotropic instability may also influence the mesoscale eddy generation by releasing energy via the horizonal velocity shear of the background flow. A dominant barotropic instability control of eddy variation has already been reported in previous studies in several ocean sectors, such as the Gulf Stream (Kang et al., 2016), the Kuroshio Extension (Yang and Liang 2018) and the Caribbean Sea (Jouanno et al., 2012). Up to now, the relative contribution from baroclinic instability and barotropic instability to the seasonal mesoscale eddy variability in the SCS, especially in the above-mentioned three EKE hotspots, is still unclear.

Apart from internal instability processes, external atmospheric forcing is also considered as an important factor influencing the eddy variation in the ocean. For instance, Yang et al. (2013) argued that the seasonal variability of EKE over the SCS, especially in the SEV region, is modulated by wind forcing. It should be noted that their argument is simply based on the high correlation between the seasonal series of EKE and the total wind power input into the surface current (i.e., the product of the wind stress vector and the surface current velocity). However, it has been well recognized that most of the wind power input does not directly go into the mesoscale eddies; it tends to first drive the large-scale flow which then transfers energy to the mesoscale eddies via internal instability processes (e.g., Cheng and Qi 2010; Von Storch et al., 2012). The direct energy exchange between the wind and the mesoscale eddies, as well as its relationship with the seasonal eddy variability in the SCS, remain to be explored.

In this study, using a new functional analysis tool, namely, Multiscale Window Transform (MWT; Liang and Anderson, 2007), we distinguish three ranges of scales, or "scale windows", a term introduced by Liang and Anderson (2007). These scale windows are the background flow window, the mesoscale eddy window and the synoptic eddy window (see section 3 for illustration). Here the synoptic eddy window is defined for high-frequency processes with periods shorter than one month. Previous studies based on high-resolution simulations have reported that high-frequency motions within this frequency band, such as frontal waves, could impact the lower-frequency mesoscale eddies through strong inverse cascades of kinetic energy (e.g., Sérazin et al., 2018; Yang and Liang 2019). The dynamical interaction between these synoptic variabilities and the mesoscale eddies remains unclear in the SCS. In order to investigate the instability nature and the multiscale interactions underlying the seasonal mesoscale eddy variations in the SCS, we further use the MWT-based theory of canonical transfer (Liang 2016) to quantify and understand these processes.

This paper is organized as follows. Section 2 describes the data used in this work. Section 3 gives a brief introduction of MWT and the MWT-based theory of canonical transfer. We examine the seasonal variability of the mesoscale EKE in the SCS in section 4.1, with the main focus on the three identified regions. Diagnoses of multiscale interactions associated with baroclinic and barotropic instabilities, as wells as the energy transfers between the mesoscale and the synoptic eddies are shown in sections 4.2 and section 4.3. Moreover, the external wind work done to oceanic mesoscale eddies is examined in section 4.4. This study is summarized in section 5.

2. Data

Satellite observations have offered an unpreceded measure of the global surface geostrophic currents. In this study, the altimetry data

from Archiving, Validation, and Interpretation of Satellite Oceanographic (AVISO) is utilized to examine the spatial and seasonal variations of surface mesoscale EKE in the SCS over a duration of 22 years from 1994 to 2015. The dataset has a $1/4°$ spatial resolution and a daily time interval, capable of resolving most mesoscale eddies in the ocean (Chelton et al., 2011).

A shortcoming of the altimetry data is that it only provides the geostrophic velocity fields at the surface. In order to diagnose the instability matrices (see section 3 for details), we also use output from the Hybrid Coordinate Ocean Model (HYCOM; see https://hycom.org for more details) reanalysis with the same duration from 1994 to 2015. The HYCOM output has a horizontal resolution of $1/12.5°$ and 40 vertical levels, with the top 25 levels concentrated within 300 m. HYCOM reanalysis has been widely used in energetics analysis in the SCS (e.g., Zhao et al., 2016; Zhang et al., 2017; Quan et al., 2021). The global ocean forecasting system in HYCOM employs the Navy Coupled Ocean Data Assimilation (NCODA) system (Cummings 2005; Cummings and Smedstad, 2013) for data assimilation. NCODA assimilates available satellite altimeter observations, satellite, and in-situ sea surface temperature as well as in-situ vertical temperature and salinity profiles from XBTs, Argo floats and moored buoys. It should be noted that in the SCS, different from the open oceans, the available observations for data assimilation are quite limited that HYCOM reanalysis is close to a free-running case (Quan et al., 2021). Therefore, the model is by and large consistent by kinematics and dynamics in the SCS, which is feasible for our energetics analysis. Fig. 1c–d displays the long-term mean distributions of the surface mesoscale EKE in winter and summer in the SCS calculated from the HYCOM reanalysis. One can see that the spatial distribution of mesoscale EKE derived from AVISO is well captured by the HYCOM output, although the EKE is slightly underestimated in the NEN region. A more detailed verification of the HYCOM output will be provided in section 4.1.

In addition, the wind stress field from National Centers for Environmental Prediction (NCEP) Climate Forecast System Reanalysis (CFSR), by which the HYCOM is forced, is used to estimate the wind work done to the mesoscale eddies (i.e., eddy wind work).

3. Methodology

In this study, we use a recently developed functional tool called Multiscale Window Transform (MWT; Liang and Anderson, 2007) and the MWT-based theory of canonical transfer (Liang 2016) to explore the dynamical mechanisms responsible for the seasonal variability of mesoscale eddies in the SCS. MWT decomposes a function space into a direct sum of several orthogonal subspaces. Each resulting subspace contains a specific range of scales which is termed "scale window" or simply window (Liang and Anderson 2007). As mentioned in the introduction, three windows are defined in this study, namely, the background flow window, the mesoscale window and the high-frequency synoptic window. The demarcation of the three scale windows is with respect to the time domain and the choice of window bounds (cutoff periods) is based on the fact that mesoscale eddies in the SCS generally have lifetimes ranging from 30 to 240 days (e.g., Xiu et al., 2010; Zhang et al., 2019). In this study, we choose the mesoscale window as bounded by cutoff periods of 32 and 256 days. Notice that MWT requires that the number of time steps for the selection of cutoff periods be a power of 2. For a series with a time duration of τ, a scale level j corresponds to a period $2^{-j}\tau$. With this scale-window definition, processes with periods longer than 256 days are included in the nonstationary background flow window, while those with periods shorter than 32 days are included in the synoptic window. It should be noted that a scale separation implemented in the frequency domain inevitably allows other oceanic processes which are not related to physical mesoscale eddies, such as intraseasonal signals associated with Madden-Julian Oscillation (MJO), into the band-passed mesoscale window. We remark here that the mesoscale window defined in this study includes
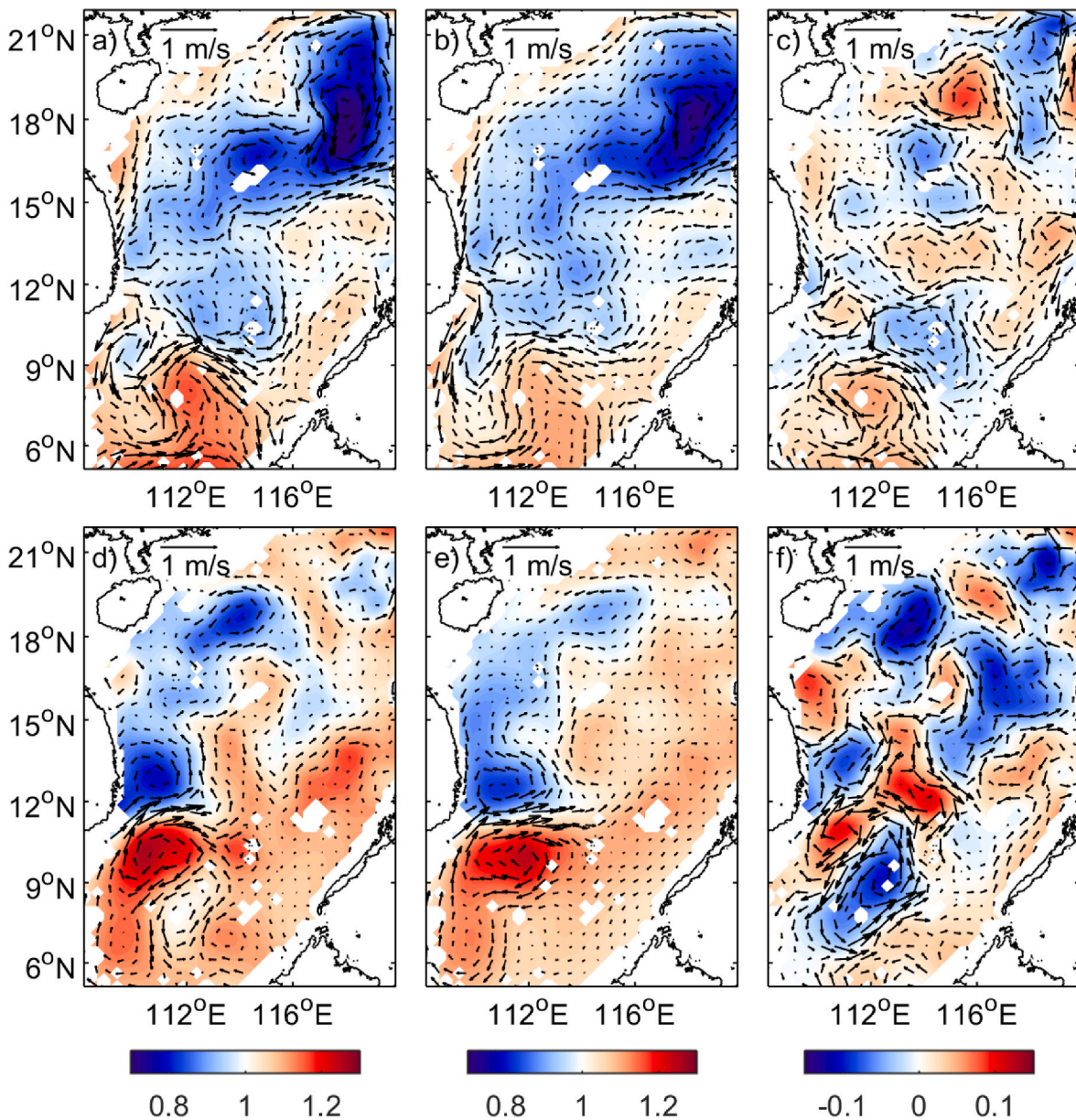
Fig. 2. The snapshots of SSH (cm) on Jan. 21, 1994 (the upper row), and Jul. 19, 1994 (the lower row). The first column represents the original SSH field simulated by HYCOM; the second and the third columns represent the SSH fields reconstructed by MWT on the background flow window and the mesoscale window, respectively.

not only the physical eddies but also contain other non-eddy processes occurring in the 32-256-day band. Fig. 2 shows the instantaneous maps of the SSH and its MWT-reconstructed fields on a winter day (Jan. 21, 1994) and a summer day (Jul. 19, 1994). One observation is that the abundant mesoscale eddies appearing in the original field are well represented in the mesoscale window. Another observation is that the background flow window successfully captures the seasonal reversal of the large-scale current. These results confirm that the cutoff periods chosen in this study are reliable.

Fig. 3 shows the variance-preserving frequency spectra of kinetic energy (KE) averaged over the SCS from AVISO (red line) and HYCOM (blue line). It can be seen that KE is mainly concentrated on the mesoscale window (the green lines mark the mesoscale window bounds), which is evident from both datasets. Besides, the fine-resolution HYCOM reanalysis allows for a representation of significant high-frequency synoptic variabilities (especially with periods shorter than one week), which is almost absent in the AVISO data due to its coarse resolution and inherent filtering.

For reference convenience, the background flow, the mesoscale and the synoptic windows are signified as $\varpi = 0, 1$ and 2, respectively.

The primary advantage of MWT is that it allows for a faithful representation of time-dependent temporal scale-based multiscale energy (or space-dependent spatial scale-based multiscale energy), which is essential for analyzing time-varying multiscale energy cycles (Liang 2016). Traditionally this is usually achieved through filtering, and simply taking the square of the filtered field as multiscale energy. Unfortunately, this is wrong even in concept. To illustrate, suppose that a time series $S(t)$ has a simple Fourier expansion with only two frequencies ω_0 and ω_1:

$$S(t) = \underbrace{(a_0 \cos \omega_0 t + b_0 \sin \omega_0 t)}_{\bar{S}} + \underbrace{(a_1 \cos \omega_1 t + b_1 \sin \omega_1 t)}_{S'}. \quad (1)$$

Here we suppose $\omega_0 \ll \omega_1$ so that the low- and high-frequency components (denoted as $\bar{S}$ and S', respectively) can be well separated. We know that the energies for the low-frequency and high-frequency parts
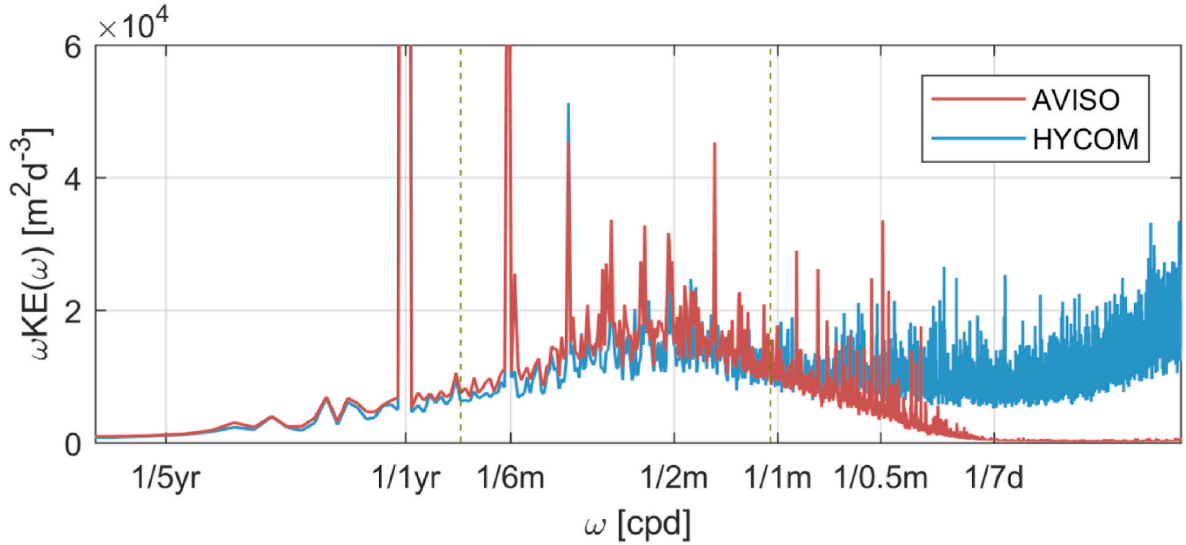
Fig. 3. Variance-preserving frequency spectra of KE averaged over the SCS based on AVISO (solid red line) and HYCOM (solid blue line). The dashed green lines denote the periods of 32 and 256 days, respectively. The range of the ordinate is limited to $0 - 6 \times 10^4$ m^2/d^3 in order to highlight the high-frequency spectra.

should be $a_0^2 + b_0^2$ and $a_1^2 + b_1^2$ (up to $\frac{1}{2}$), respectively, i.e., the square of the respective Fourier coefficients. They are absolutely not equal to the square of the reconstructed (filtered) fields, i.e., $\overline{S}^2$ and $S'2$. That is to say, multiscale energy is a concept with the transform coefficients defined in phase space instead of physical space!

Another common practice to retain the localization of multiscale energetics is by removing the averages in the classical Reynolds decomposition-based energy equation. This is also conceptually wrong. In the above example, when $\overline{S}$ is a constant (i.e., time mean), Eqn. (1) then reduces to the Reynolds' mean-eddy decomposition. The eddy energy is, by Parseval relation in functional analysis, $(a_1^2 + b_1^2) = \overline{S'2}$. So the overbar which denotes time-averaging cannot be simply removed. From this example, one could see why the representation of multiscale energy in the classical formalism must be in a global or integral form, which however leads to the loss of localization and hence cannot be used for the study of processes intermittent in time and space.

The above problem is actually a very fundamental one, which however has been overlooked in atmosphere-ocean science for decades. The development of MWT (Liang and Anderson 2007) is just for the tackling of it. Liang and Anderson found that, for a class of specially devised orthogonal filters, there exists a transform-reconstruction pair, which is the MWT and its counterpart, multiscale window reconstruction (MWR). The latter is just like a filtered property. In other words, for each MWR/filtered variable $S_n^{\sim\varpi}$, there is a corresponding transform coefficient (n denotes the discrete time step in the sampling space). The multiscale energy on window ϖ proves to be $(\widehat{S_n^{\sim\varpi}})^2$ (cf. Liang and Anderson 2007). Within the MWT framework, the multiscale KE and available potential energy (APE) on window ϖ can be expressed as

$$K^\varpi = \frac{1}{2}\widehat{\mathbf{v}}_h^{\sim\varpi} \cdot \widehat{\mathbf{v}}_h^{\sim\varpi} \tag{2}$$

and

$$A^\varpi = \frac{g^2}{2\rho_0^2 N^2}(\widehat{\rho}^{\sim\varpi})^2 \tag{3}$$

where $\mathbf{v}_h$ is the horizontal velocity, ρ_0 the constant reference density (= 1025 kg/m^3), N the buoyancy frequency and ρ the density perturbation over a reference density profile (chosen as the time and area mean of the density). The subscript n (time step) is omitted for notational brevity. Similarly, the rate of eddy wind work (EWW) could also be obtained

Table 1
Mathematical expressions and physical interpretations of the energetic terms in Eqs. (5) and (6). For more details, refer to Liang (2016).

Term	Mathematical expression	Physical interpretation
K^ϖ	$\frac{1}{2}\widehat{\mathbf{v}}_h^{\sim\varpi} \cdot \widehat{\mathbf{v}}_h^{\sim\varpi}$	Kinetic energy on scale window ϖ
Γ_K^ϖ	$\frac{1}{2}[\widehat{(\mathbf{vv}_h)}^{\sim\varpi} : \nabla\widehat{\mathbf{v}}_h^{\sim\varpi} - \nabla\cdot\widehat{(\mathbf{vv}_h)}^{\sim\varpi} \cdot \widehat{\mathbf{v}}_h^{\sim\varpi}]$	Canonical transfer of kinetic energy to scale window ϖ
Q_K^ϖ	$\frac{1}{2}\widehat{(\mathbf{vv}_h)}^{\sim\varpi} \cdot \widehat{\mathbf{v}}_h^{\sim\varpi}$	Kinetic energy flux on scale window ϖ
Q_P^ϖ	$\frac{1}{\rho_0}\widehat{\mathbf{v}}^{\sim\varpi}\widehat{P}^{\sim\varpi}$	Pressure flux on scale window ϖ
b^ϖ	$\frac{g}{\rho_0}\widehat{\rho}^{\sim\varpi}\widehat{w}^{\sim\varpi}$	Buoyancy conversion on scale window ϖ
A^ϖ	$\frac{g^2}{2\rho_0^2 N^2}(\widehat{\rho}^{\sim\varpi})^2$	Available potential energy on scale window ϖ
Γ_A^ϖ	$\frac{g^2}{2\rho_0^2 N^2}[\widehat{(\mathbf{v}\rho)}^{\sim\varpi} \cdot \nabla\widehat{\rho}^{\sim\varpi} - \widehat{\rho}^{\sim\varpi}\nabla\cdot\widehat{(\mathbf{v}\rho)}^{\sim\varpi}]$	Canonical transfer of available potential energy to scale window ϖ
Q_A^ϖ	$\frac{g^2}{2\rho_0^2 N^2}\widehat{\rho}^{\sim\varpi}\widehat{(\mathbf{v}\rho)}^{\sim\varpi}$	Available potential energy flux on scale window ϖ
F_K^ϖ, F_A^ϖ	–	Residue terms including forcing and dissipation processes.

through MWT:

$$\text{EWW} = \frac{1}{\rho_0}\widehat{\mathbf{v}}_0^{\sim 1} \cdot \widehat{\boldsymbol{\tau}}^{\sim 1} \tag{4}$$

where $\mathbf{v}_0$ is the surface horizontal velocity and $\boldsymbol{\tau}$ the surface wind stress. The superscript 1 denotes that the calculation is on the mesoscale window ($\varpi = 1$).

From the primitive equations, Liang (2016) derived the equations of KE and APE on window ϖ as follows:

$$\frac{\partial K^\varpi}{\partial t} = \Gamma_K^\varpi - \nabla\cdot Q_K^\varpi - \nabla\cdot Q_P^\varpi + b^\varpi + F_K^\varpi, \tag{5}$$

$$\frac{\partial A^\varpi}{\partial t} = \Gamma_A^\varpi - \nabla\cdot Q_A^\varpi - b^\varpi + F_A^\varpi. \tag{6}$$

The definition of each term is referred to Table 1. A complete derivation of the formulas is referred to Liang (2016). In Eqs. (5) and (6), the Γ terms are the energy transfers across different scale windows.
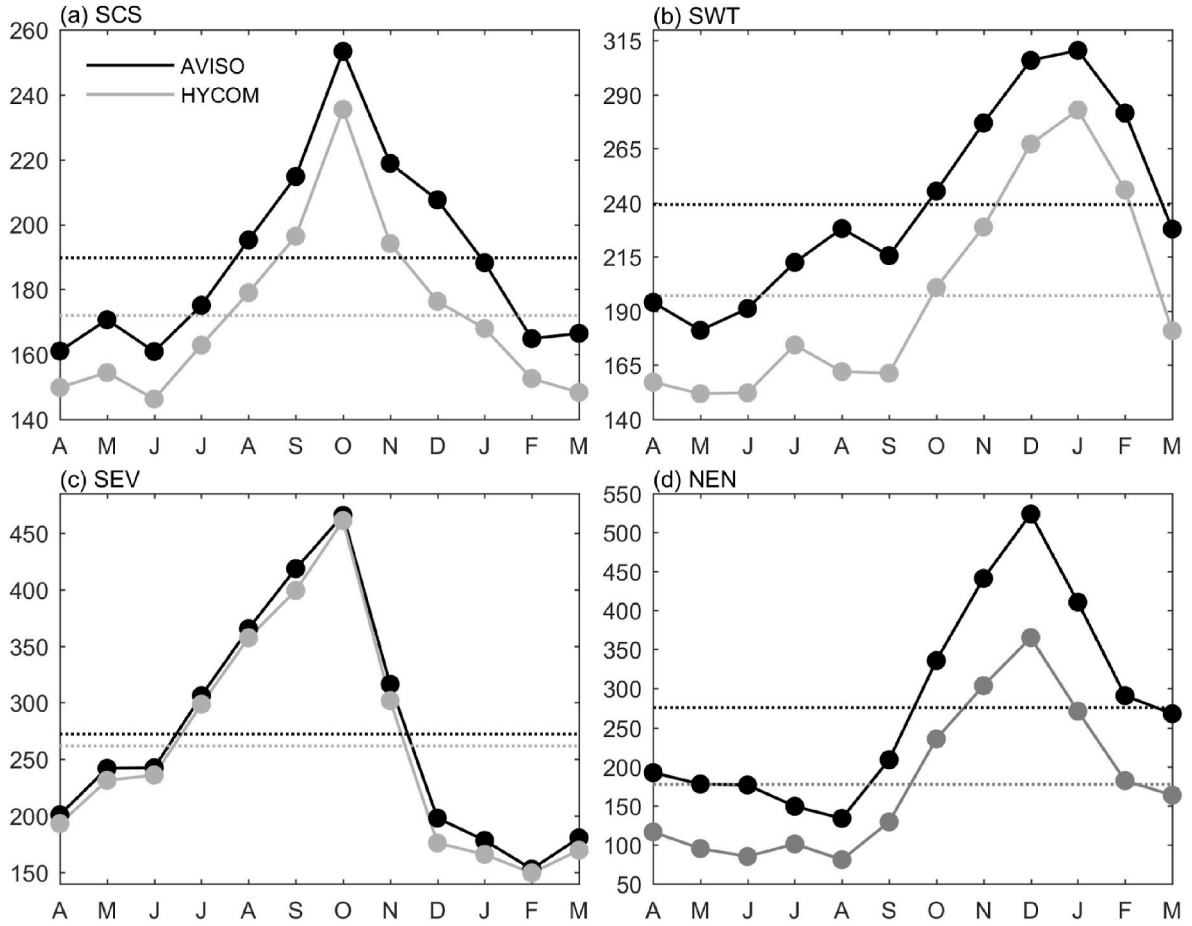
Fig. 4. Climatological annual cycles of surface mesoscale EKE (cm^2/s^2) averaged over (a) the whole SCS, (b) SWT, (c) SEV and (d) NEN calculated from AVISO (black solid lines) and HYCOM (grey solid lines). The black and grey dashed lines denote the long-term mean levels of mesoscale EKE averaged over each domain based on AVISO and HYCOM, respectively.

Specifically, Γ_K^ϖ (Γ_A^ϖ) is the transfer of KE (APE) to window ϖ from all windows. Liang (2016) proved that the Γ terms possess an important property:

$$\sum_\varpi \sum_n \Gamma_n^\varpi = 0, \tag{7}$$

which states that the transfer process is conserved in the space of scale, without generating or losing energy as a whole. Although simple to state, this property does not hold in classical energetics formalisms. To distinguish, Γ is termed "canonical transfer" (Liang, 2016). Canonical transfer is of key importance because it is closely related to the GFD concept, namely, instability. By the classical definition of baroclinic instability and barotropic instability (e.g., Pedlosky 1979), Liang and Robinson (2007) rigorously proved that the canonical transfer of KE and that of APE correspond precisely to barotropic instability and baroclinic instability, respectively. They also showed that, for a benchmark barotropic model whose instability structure is analytically known, the

traditional formalism fails to give the correct source of instability, while canonical transfer does. It should be noted that the canonical KE (APE) transfer matrix comprises contribution from the vertical shear of the velocity (density), as shown in Table 1, which does not exist under quasi-geostrophic assumption. Nevertheless, such contribution is found one order of magnitude smaller than its horizontal counterpart in our analysis, and therefore is not further distinguished in this study.

Notice that Γ_K^ϖ and Γ_A^ϖ in Eqs. (5) and (6) are still in cumulated forms. They need to be further decomposed to obtain the window-window interactions within the three-scale window framework. This procedure is called the "interaction analysis" (Liang & Robinson 2005). As shown in Eqn. (8), the canonical transfer can be written as a linear combination of terms in the form

$$\Gamma_n^\varpi = \widehat{\Re}_n^{\tilde{}\varpi}\,(\widehat{pq})_n^{\tilde{}\varpi}. \tag{8}$$

It therefore suffices to analyze this single term. Take Γ_n^1 for example,

$$\Gamma_n^1 = \widehat{\Re}_n^{\tilde{}1}(\widehat{pq})_n^{\tilde{}1} = \widehat{\Re}_n^{\tilde{}1}\left(\sum_{\varpi_1=0}^{2} p^{\tilde{}\varpi_1}\sum_{\varpi_1=0}^{2} q^{\tilde{}\varpi_1}\right)_n^{\tilde{}1} = \widehat{\Re}_n^{\tilde{}1}\left[\left(p^{\tilde{}0}\widehat{q^{\tilde{}0}}\right)_n^{\tilde{}1} + \left(p^{\tilde{}0}\widehat{q^{\tilde{}1}}\right)_n^{\tilde{}1} + \left(p^{\tilde{}1}\widehat{q^{\tilde{}0}}\right)_n^{\tilde{}1}\right] + \widehat{\Re}_n^{\tilde{}1}\left[\left(p^{\tilde{}1}\widehat{q^{\tilde{}2}}\right)_n^{\tilde{}1} + \left(p^{\tilde{}2}\widehat{q^{\tilde{}1}}\right)_n^{\tilde{}1} + \left(p^{\tilde{}2}\widehat{q^{\tilde{}2}}\right)_n^{\tilde{}1}\right]$$

$$+ \widehat{\Re}_n^{\tilde{}1}\left[\left(p^{\tilde{}0}\widehat{q^{\tilde{}2}}\right)_n^{\tilde{}1} + \left(p^{\tilde{}2}\widehat{q^{\tilde{}0}}\right)_n^{\tilde{}1}\right] + \widehat{\Re}_n^{\tilde{}1}\left(p^{\tilde{}1}\widehat{q^{\tilde{}1}}\right)_n^{\tilde{}1}. \tag{9}$$
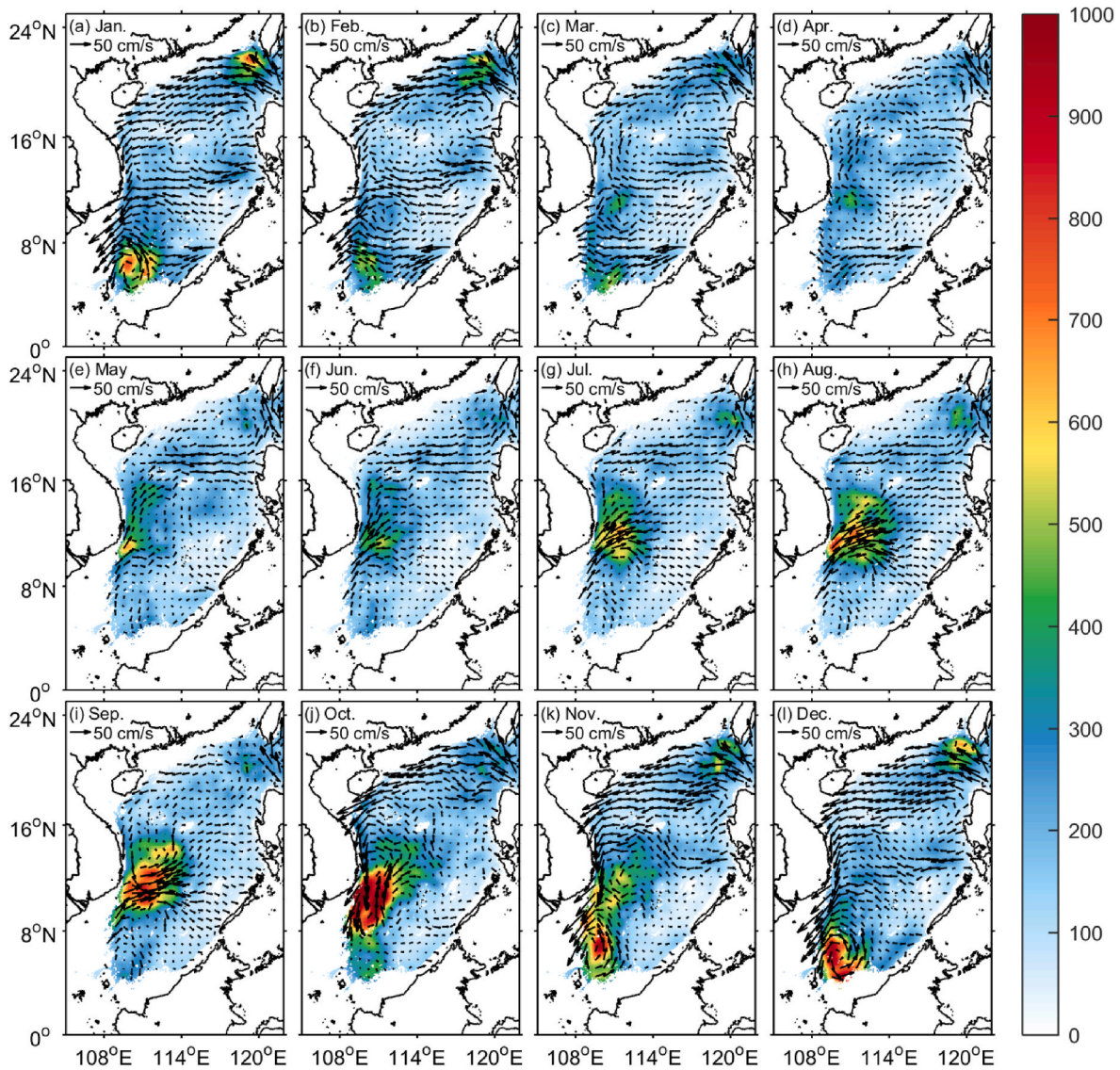
Fig. 5. Climatological monthly maps of currents (arrows; cm/s) and mesoscale EKE (shadings; cm^2/s^2) at the surface calculated from AVISO.

The first two terms on the right-hand side of Eqn. (9) stand for the energy transfers to window 1 from window 0 and window 2, respectively. Symbolically, they can be written as $\Gamma_n^{0\to1}$ and $\Gamma_n^{2\to1}$. The two scale windows may also combine to contribute to Γ_n^1, though generally the contribution is negligible; this makes the third term, or $\Gamma_n^{0\oplus2\to1}$ for short. The last term, $\widehat{\mathfrak{R}}_n^{\sim1}(p^{\widetilde{\sim1}}q^{\sim1})_n^{\sim1}$ is the transfer from window 1 itself. Now for scale window 1, $\Gamma_n^{0\to1}$ and $\Gamma_n^{2\to1}$ are selected out of Γ_n^1. Readers are referred to Liang and Robinson (2005) and Liang (2016) for details. The resulting $\Gamma_K^{0\to1}$ denotes the canonical transfer of KE from the background flow window to the mesoscale window; $\Gamma_A^{0\to1}$ denotes the canonical transfer of APE from the background flow window to the mesoscale window. A positive $\Gamma_A^{0\to1}$ ($\Gamma_K^{0\to1}$) is indicative of the occurrence of baroclinic (barotropic) instability. By taking advantage of the three-scale framework, the scale interactions between the synoptic eddies and the mesoscale eddies can also be quantified, which are measured by $\Gamma_A^{2\to1}$ and $\Gamma_K^{2\to1}$. A positive $\Gamma_A^{2\to1}$ or $\Gamma_K^{2\to1}$ indicates an inverse cascade of APE or KE from the high-frequency synoptic eddies to the lower-frequency mesoscale eddies, respectively, and vice versa.

4. Results

4.1. Seasonal variability of the mesoscale EKE in the SCS

In this section the seasonality of the mesoscale EKE and its spatial difference in the SCS are examined. Fig. 4 depicts the climatological seasonal cycles of surface mesoscale EKE (K^1) averaged over the whole SCS and the three EKE centers (framed by the three black boxes in Fig. 1a–b) based on AVISO (solid black line) and HYCOM (solid grey line). The dashed lines in each subplot denote the long-term mean levels of the surface K^1 in the respective region. Considering that the area-mean results may be sensitive to the size of the selected boxes, we carried out a series of sensitivity experiments to validate our region selection (not shown). The results confirm that the seasonal cycles of the relevant energetic processes as shown below are not sensitive to a slight change of the box size in all three considered subdomains as long as the maxima of EKE are included in the chosen boxes. The AVISO-based annual cycles of K^1 in Fig. 4 show that mesoscale EKE in the SCS bears pronounced seasonal variability. The HYCOM reanalysis successfully reproduces the seasonal cycles of K^1 in the whole SCS as well as in the three subdomains, suggesting that the model output is reliable for our purpose. In the three subregions (Fig. 4c–d), the seasonal cycles of
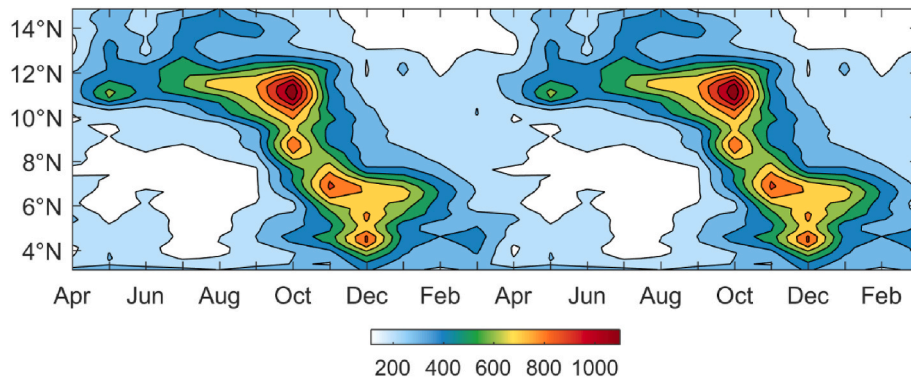
Fig. 6. Latitude-time plot of the surface mesoscale EKE (cm^2/s^2) from satellite altimeter.

surface mesoscale EKE show different phases, with maxima of K^1 attained in January, October and December in the SWT, SEV and NEN regions, respectively.

Specifically, the seasonal variability of mesoscale eddies in the SWT region is characterized by strong (weak) K^1 from October through February (from March through September). This K^1 annual cycle is consistent with previous studies reporting that the eddy activity in the northeastern SCS is much stronger in winter than summer (e.g., Cheng
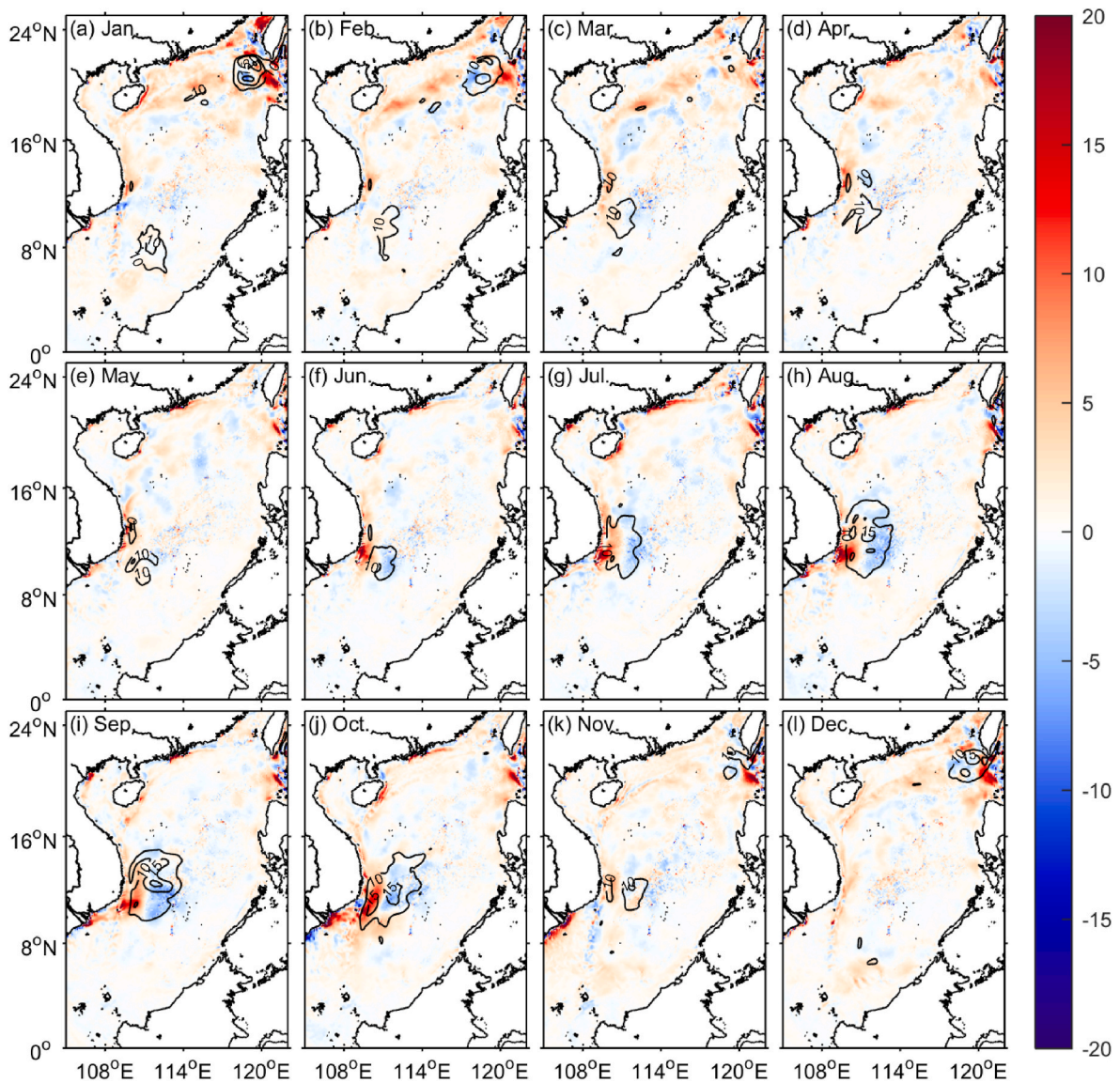

Fig. 7. Climatological monthly maps of $\Gamma_A^{0\to1}$ (shadings; cm^3/s^3) and K^1 (contours; m^3/s^2) vertically integrated from surface to bottom. K^1 is contoured only when it is equal to or larger than 10 m^3/s^2.

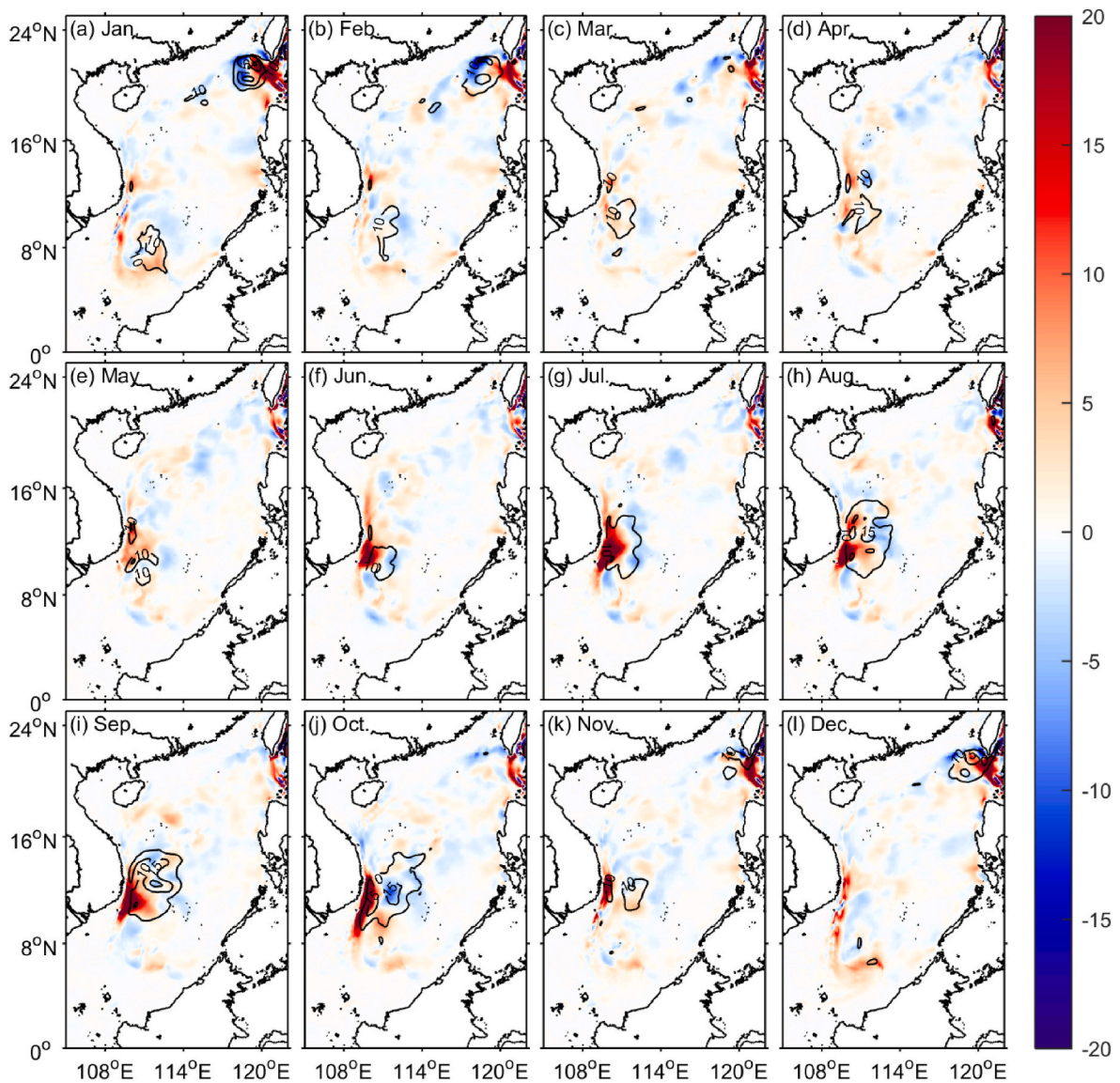**Fig. 8.** As in Fig. 7 but for $\Gamma_K^{0 \to 1}$.

and Qi 2010; Yang et al., 2013). Fig. 5 displays the long-term mean circulation (arrows) and K^1 (shadings) at the surface in each month from satellite observation. The figure shows that the mesoscale EKE in the SWT region is mainly distributed around the Kuroshio intrusion region, and the amplitude of the mesoscale EKE seems to covary with the intensity of the Kuroshio intrusion. Over the duration of high K^1 from October through February, intense Kuroshio intrusion occurs with a direct branch extending into the interior SCS and a large loop returning to the Pacific, providing an intensified background flow favorable for the growth of perturbations. Particularly, the K^1 reaches a peak of 811 cm^2/s^2 in January when Kuroshio exhibits the most intense intrusion throughout the year (Fig. 5a). On the contrary, when the intensity of Kuroshio intrusion is decreased, K^1 in the SWT region is also weakened.

The phase of the K^1 seasonal variability in the SEV region is quite different from that in the SWT region; it is enhanced from July through November and remains low levels in other months, consistent with Wang et al. (2012). A closer look at the corresponding current fields (Fig. 5) indicates that strong K^1 in the SEV region is mainly distributed along the SVOC. Since June as the SVOC becomes stronger and extends further eastward, K^1 is strengthened as well. In September, the circulation pattern in the SCS begins to change due to the transition of the

monsoon. The southward flowing SCSWBC forms by October, giving rise to a sharp V-shaped bend near 10°N with strong shear of horizontal velocity (Fig. 5j). As a result, a large number of eddies may form in the vicinity of the bend, leading to the strongest mesoscale EKE in the SEV region throughout the year (Fig. 4c). In November, the southward SCSWBC continues to develop and the SVOC disappears. Consequently, K^1 dramatically drops to the July-level in November (Fig. 4c). In the next few months, the winter circulation takes control and meanwhile K^1 continues to decrease.

As for the region of NEN, K^1 is noticeably intensified from October through February (Fig. 4d). The K^1 estimated from AVISO reaches a peak of 523.77 cm^2/s^2 in December, nearly 1.8 times as high as the mean K^1 level. The seasonality of the mesoscale eddies in this region is not well noted previously as those in the SEV and SWT regions. As we can see from Fig. 5, strong K^1 in the NEN region corresponds well with the intense background flow here. During the period from November to January, the SCSWBC turns anticlockwise and forms a cyclonic circulation in the NEN region. Overall, K^1 concentrates around the cyclonic circulation and modulates in pace with the evolution of the background flow. The strength of the cyclonic circulation is maximized in December, corresponding to the December peak of K^1 (Fig. 4d). The following collapse of the winter circulation leads to the decline of K^1; mesoscale
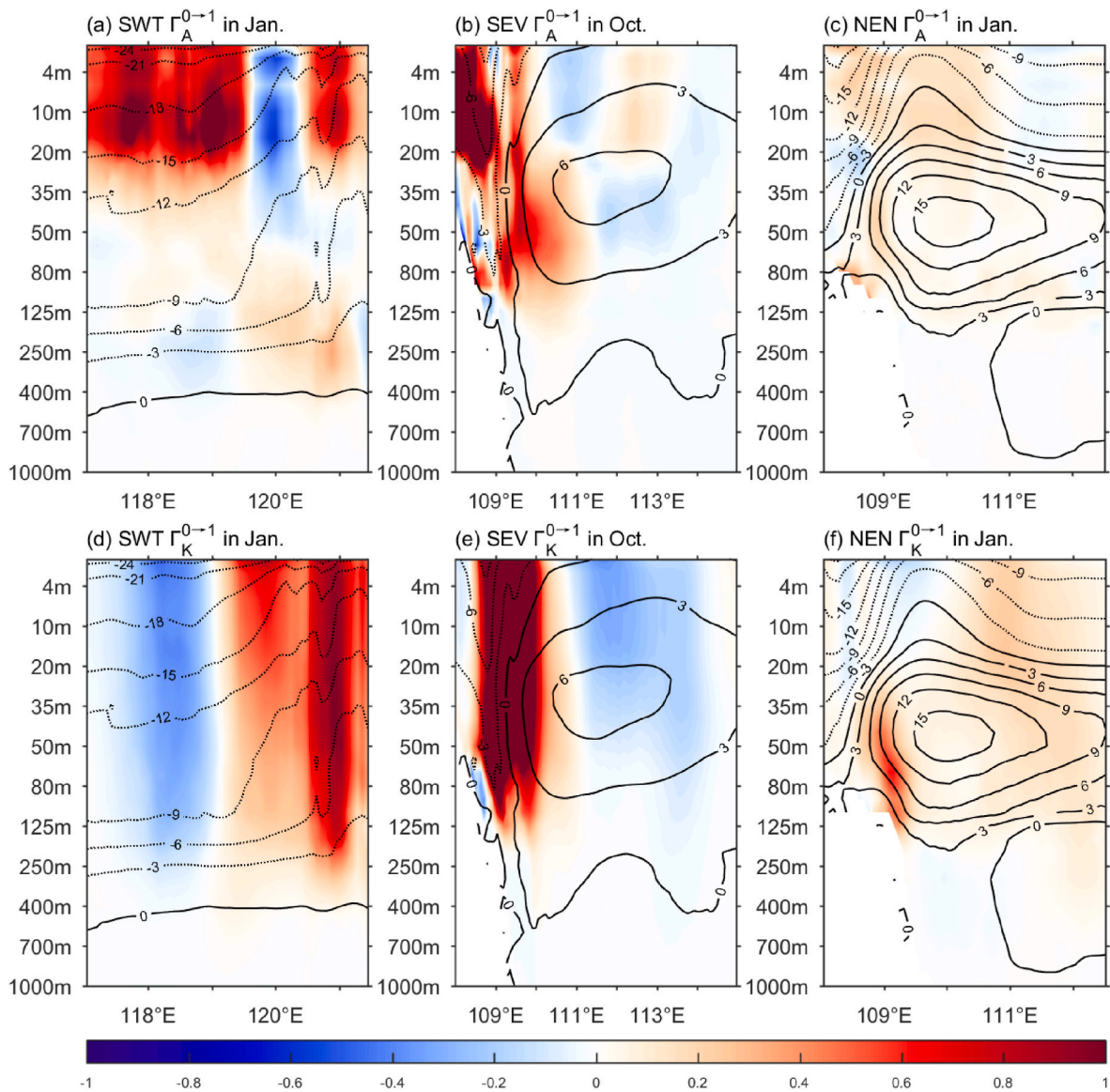
Fig. 9. Long-term mean vertical structures of $\Gamma_A^{0\to1}$ (upper row; 10^{-3} cm^2/s^3) and $\Gamma_K^{0\to1}$ (lower row; 10^{-3} cm^2/s^3) along with zonal velocity (cm/ s) meridionally averaged over the subdomains as marked in Fig. 1 in peak months of the depth-integrated K^1 (January in SWT, September in SEV and January in NEN). The left, middle and right columns are for the SWT, SEV and NEN regions, respectively.

eddies are inactive until the cyclonic circulation reappears in next winter.

It is noticeable that the high K^1 centers in the SEV and the NEN regions are closely connected geographically, and they maybe also related dynamically. According to the altimeter-based spatial-temporal variation of K^1 shown in Fig. 6, significant signals of high K^1 appear in the SEV region in summer and propagate southward to the NEN region during autumn when transition of the SCS circulation occurs (Gan et al., 2006). On the contrary, no northward propagation of the K^1 signals from the NEN to the SEV regions are found in spring when another circulation transition undergoes. The asymmetry of the K^1 propagation in the southwestern SCS may be related to the different transition processes in autumn and spring of the background flow, namely the SCSWBC. What kind of dynamical processes are responsible for the signals of mesoscale EKE propagating southward in autumn and what kind of role the SCSWBC plays in these processes are intriguing questions for future investigation.

In conclusion, mesoscale EKE in the SCS exhibits remarkable seasonal variability. The annual cycles of surface K^1 averaged over the three

identified high-K^1 centers, namely SWT, SEV and NEN, are not in the same phase, with peaks appearing in January, October and December, respectively. As expected, eddies in these regions are vigorous when strong background flow develops, suggesting that mesoscale eddies may gain energy from the background flow through instability processes. Since the HYCOM reanalysis captures the K^1 seasonality rather well, we will use this dataset to quantify the roles of baroclinic and barotropic instabilities in modulating the mesoscale EKE seasonal cycles in the SCS.

4.2. Baroclinic and barotropic instabilities

We first examine the role of baroclinic instability in governing the mesoscale eddy variations in the SCS. As introduced in section 3, baroclinic instability can be quantified by the $\Gamma_A^{0\to1}$ matrix. Recall that positive $\Gamma_A^{0\to1}$ is indicative of the occurrence of baroclinic instability. Fig. 7 illustrates the climatological monthly distributions of the vertically integrated $\Gamma_A^{0\to1}$ (shadings). The depth-integrated K^1 equal to or larger than 10 m^3/s^2 is contoured in black. The vertical integral in this study is made from surface to bottom. We also tried to do the integral

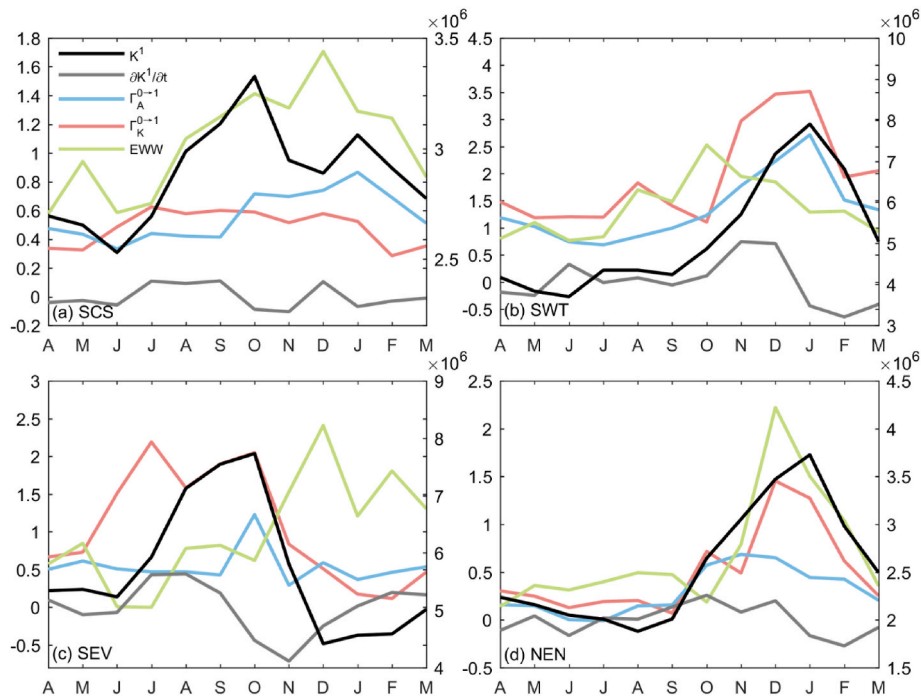**Fig. 10.** Climatological annual cycles of K^1 (black lines; cm^3/s^2), $\partial K^1/\partial t$ (gray lines; cm^3/s^3) $\Gamma_A^{0\rightarrow1}$ (blue lines; cm^3/s^3), $\Gamma_K^{0\rightarrow1}$ (red lines; cm^3/s^3) and EWW (green lines; cm^3/s^3) horizontally averaged over (a) the whole SCS, (b) SWT, (c) SEV and (d) NEN based on HYCOM. The first four terms are vertically integrated from surface to bottom. The ordinate for K^1 is on the right side, and the ordinate for the other terms is on the left side in each subplot.

from surface to 750 m and found that the result is almost the same, implying that the eddy energies have small amplitudes in the deep layer, which is consistent with the argument in a recent study on the eddy energy in the SCS (Li et al., 2021). The $\Gamma_A^{0\rightarrow1}$ pattern in Fig. 7 reveals that significant signals are distributed in the SWT and SEV regions. The amplitudes of $\Gamma_A^{0\rightarrow1}$ in these two regions get strengthened during periods of strong K^1 (December–February in SWT and July–October in SEV) and get weakened in other months when local K^1 is decreased. The collocation and covariation of $\Gamma_A^{0\rightarrow1}$ and K^1 suggest that the seasonal variability of mesoscale eddies in these two regions are controlled by baroclinic instability, which acts to extract APE from the background flow (i.e., the Kuroshio intrusion and the SVOC) to the mesoscale eddies. In the NEN region, the signal of $\Gamma_A^{0\rightarrow1}$, though in small amplitude, is strengthened during high-K^1 period from October through February, indicating that the cyclonic circulation mentioned in section 4.1 is baroclinically unstable during this period. The small amplitude of $\Gamma_A^{0\rightarrow1}$ in NEN indicates that baroclinic instability is not the dominant process responsible for the strong mesoscale EKE in this region. The above results suggest that baroclinic instability is responsible for the seasonal variations of the mesoscale eddies in all three considered subregions with high EKE levels. This is consistent with the classical view of eddy generation via baroclinic instability (e.g., Ferrari and Wunsch 2009; Storch et al., 2012).

In the following, we examine another eddy generation mechanism, i. e., barotropic instability, to see its role in modulating the seasonal variations of mesoscale EKE in the three regions. As introduced in section 3, barotropic instability is quantified by the canonical transfer $\Gamma_K^{0\rightarrow1}$ matrix. Fig. 8 shows the climatological monthly patterns of the vertically integrated $\Gamma_K^{0\rightarrow1}$ in the SCS. Strong positive $\Gamma_K^{0\rightarrow1}$ can be found in all the three subregions (SWT, SEV and NEN), especially during the months when local EKE level is high (Fig. 8), indicative of the occurrence of barotropic instability in these regions. For instance, $\Gamma_K^{0\rightarrow1}$ in the SWT region is strengthened in November through February when the mesoscale activities are enhanced, and it is weakened in other months when the mesoscale activities are relatively low. It is maximized in January

(Fig. 8a), indicating that the background flow (i.e., the Kuroshio intrusion) is most barotropically unstable in January, corresponding to the K^1 peak at this time. The similarity between the seasonal variations of $\Gamma_K^{0\rightarrow1}$ and K^1 in each subregion suggests that barotropic instability which has been neglected in the energetics study in the SCS plays a role in modulating the seasonal mesoscale activities. The seasonal modulation of mesoscale eddies by barotropic instability in the high-K^1 centers can be described as below. Take the SEV region as an example. As the background flow in this region, namely the SVOC develops and gradually get strengthened, barotropic instability of the SVOC is also increased due to the strengthened horizontal velocity shear. Strong barotropic instability of the SVOC transfers KE to mesoscale eddies and finally leads to the vigorous mesoscale activities in this region. Afterwards, the SVOC decays and barotropic instability get weakened; correspondingly, the mesoscale activities are depressed.

A closer look at Figs. 7 and 8 reveals spatial variations of $\Gamma_A^{0\rightarrow1}$ and $\Gamma_K^{0\rightarrow1}$ inside the high-K^1 centers. It shows that the three considered subregions, especially the SWT and SEV regions, are mostly occupied by positive canonical transfers with patches of negative transfers embedded. This spatial pattern suggests that baroclinic and barotropic instabilities do not occur everywhere within the high-K^1 centers. To further examine the spatial patterns of baroclinic and barotropic transfers, we plot in Fig. 9 the vertical structures of $\Gamma_A^{0\rightarrow1}$ and $\Gamma_K^{0\rightarrow1}$ in the three selected regions when local K^1 peaks. It reveals that the baroclinic transfer $\Gamma_A^{0\rightarrow1}$ is dominantly positive in the three regions (Fig. 9a–c), indicating that the background flows are generally baroclinically unstable. While patches of negative $\Gamma_A^{0\rightarrow1}$ are scattered in each region, they are negligible with small amplitude and limited area. Different from $\Gamma_A^{0\rightarrow1}$, the barotropic transfer $\Gamma_K^{0\rightarrow1}$ in SWT and SEV shows clear spatial difference along zonal direction (Fig. 9d–e). For the SWT region, $\Gamma_K^{0\rightarrow1}$ tends to be positive in the east SWT and negative in the west SWT. For the SEV region, positive (negative) $\Gamma_K^{0\rightarrow1}$ is found in the near-shore (offshore) region. Such patterns imply that in the east SWT and the near-shore region in SEV the background flows provide KE for the growth of mesoscale eddies via barotropic instability. On the contrary, the
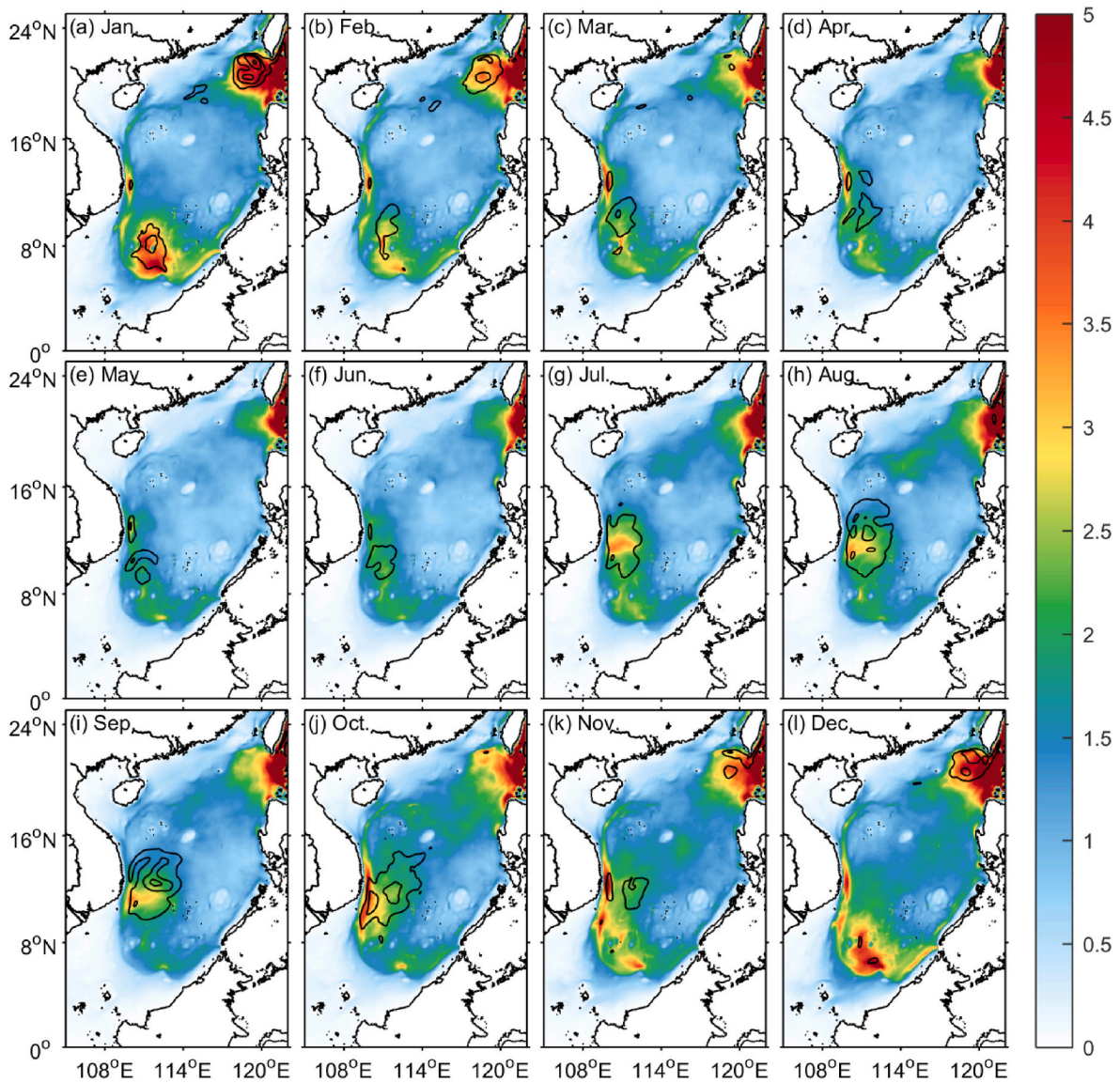
Fig. 11. Climatological monthly maps of K^2 (shadings; m^3/s^2) vertically integrated from surface to bottom based on HYCOM. The depth-integrated K^1 (contours; m^3/ s^2) equal to or larger than 10 m^3/s^2 is contoured.

background flows in the west SWT and the off-shore region in SEV extract KE from mesoscale eddies to replenish themselves; the inverse cascade of KE suggests that other processes such as nonlocal transport process as shown in Eqn. (5) could be responsible for the strong K^1 in these regions. Nevertheless, Fig. 9d–e shows that positive $\Gamma_K^{0\rightarrow1}$ has much larger amplitude than negative $\Gamma_K^{0\rightarrow1}$ does in both SWT and SEV, indicative of the dominant role played by barotropic instability. Along with the overall mixed instability in NEN implied by the positive $\Gamma_A^{0\rightarrow1}$ and $\Gamma_K^{0\rightarrow1}$ shown in Fig. 9c and f respectively, our conclusion is that the background flows in the three high-K^1 centers are dominantly baroclinically and barotropically unstable.

Comparing the baroclinic and barotropic transfers $\Gamma_A^{0\rightarrow1}$ and $\Gamma_K^{0\rightarrow1}$ from both horizontal and vertical structures as shown in Figs. 7–9, we find that $\Gamma_K^{0\rightarrow1}$ appears to have larger amplitude than $\Gamma_A^{0\rightarrow1}$. To quantitively determine the relative importance of baroclinic and barotropic instabilities to the seasonal mesoscale eddy activities in the SCS, we plot in Fig. 10 the annual cycles of $\Gamma_A^{0\rightarrow1}$ (blue lines) and $\Gamma_K^{0\rightarrow1}$ (red lines) together with K^1 (black lines) and $\partial K^1/\partial t$ (gray lines; the temporal change rate of mesoscale EKE) averaged over the whole SCS as well as the three subdomains. Here the values of $\Gamma_A^{0\rightarrow1}$, $\Gamma_K^{0\rightarrow1}$, K^1 and $\partial K^1/\partial t$ are

all vertically integrated from surface to bottom. It can be seen that $\partial K^1/ \partial t$ and K^1 exhibit similar seasonal variations in the three focused subdomains, suggesting that both indices can be used to indicate the seasonality of mesoscale eddies in these regions. These time series confirm that barotropic instability plays a more important role in controlling the mesoscale EKE seasonal variability than baroclinic instability does in the SCS. Specifically, in the SWT region (Fig. 10b), both $\Gamma_A^{0\rightarrow1}$ and $\Gamma_K^{0\rightarrow1}$ have large amplitude and exhibit annual cycles in phase with K^1 and $\partial K^1/\partial t$. This indicates that baroclinic and barotropic instabilities, or the mixed instabilities, jointly modulate the seasonal variability of mesoscale eddies in the SWT region. In contrast, $\Gamma_K^{0\rightarrow1}$ has larger amplitude and is more correlated with $\partial K^1/\partial t$ than $\Gamma_A^{0\rightarrow1}$ does in the SEV and NEN regions (Fig. 10c–d). The above results highlight the critical role played by barotropic instability in governing the seasonal variability of mesoscale eddies in the three typical regions of SCS where local EKE levels are high. Due to the importance of barotropic instability in all three K^1 centers, $\Gamma_K^{0\rightarrow1}$ averaged over the whole SCS (Fig. 10a) is enhanced in most high-K^1 months. On the contrary, since baroclinic instability only plays a key role in the SWT region where K^1 peaks in January, strong $\Gamma_A^{0\rightarrow1}$ mainly shows in winter, corresponding to the second peak of K^1 in
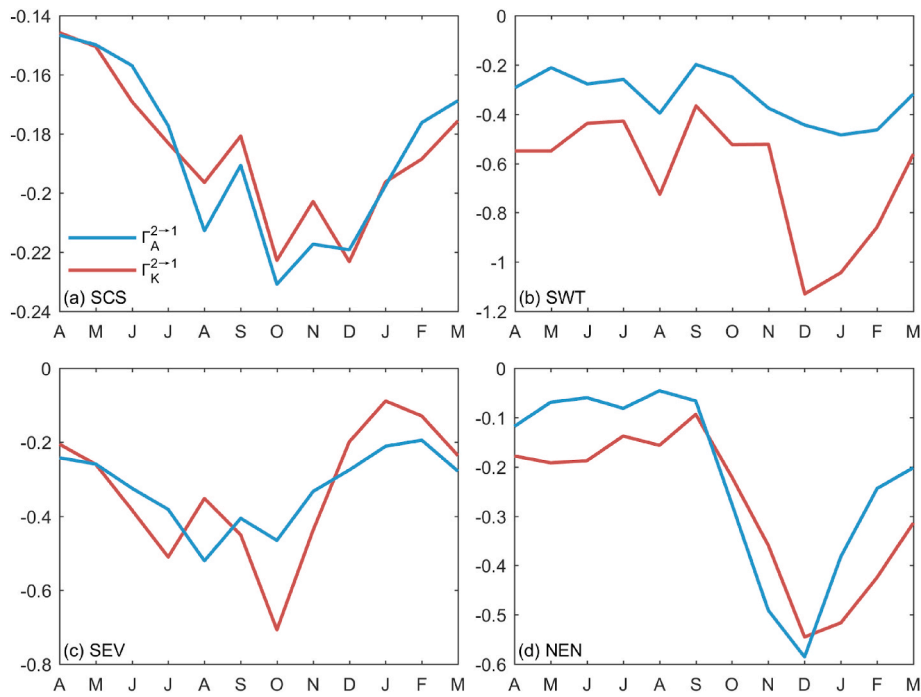
Fig. 12. Climatological annual cycles of $\Gamma_A^{2\rightarrow 1}$ (blue lines; cm^3/s^3) and $\Gamma_K^{2\rightarrow 1}$ (red lines; cm^3/s^3) vertically integrated from surface to bottom and horizontally averaged over (a) the whole SCS, (b) SWT, (c) SEV and (d) NEN calculated from HYCOM.

January.

Our results based on the MWT and the MWT-based theory of canonical transfer reveal that barotropic instability plays a key role in modulating the seasonal eddy variability in the SCS. Different from the previous argument that baroclinic instability dominates the seasonal EKE in the SCS (e.g., Chen et al., 2012; Wang et al., 2012), we find that baroclinic instability process is important only in the SWT region, but not in the SEV and the NEN regions. The different behaviors of baroclinic instability in modulating the seasonal eddy variability in the three subregions may be due to the spatial variation of the stratification in the SCS (Chen et al., 2012; Wang et al., 2012; Li et al., 2021). The stratification is found to be weak but with significant seasonal variation in the SWT region. The local weak stratification facilitates the process of baroclinic instability, and its strong seasonal variation could lead to strong seasonal variation of baroclinic instability which finally modulates the seasonal eddy generation in the SWT region. On the contrary, the stratifications in the other two regions are found to be strong but with relatively weak seasonal variation. This indicates that the strength of the baroclinic instability as well as its seasonal variation are limited in these two regions.

4.3. Mesoscale-synoptic eddy interaction

In the preceding section the interaction between background flow and mesoscale eddies is analyzed. The impact of the synoptic eddies to the seasonal variability of the lower-frequency mesoscale eddies has not been well documented. Next we focus on the mesoscale-synoptic eddy interaction based on the $\Gamma_A^{2\rightarrow 1}$ and $\Gamma_K^{2\rightarrow 1}$ matrices which correspond to APE and KE transfers from the synoptic window to the mesoscale window, thanks to the three-scale window framework. Before we explore the interaction between the mesoscale eddies and the synoptic eddies, it is necessary to firstly have a look at the distributions of synoptic eddies in the SCS. Fig. 11 displays the long-term monthly spatial patterns of synoptic EKE (K^2; shadings) vertically integrated from surface to bottom. The overlapped contours in Fig. 11 denote the depth-integrated K^1 equal to or larger than 10 m^3/s^2. Similarly, one can identify three centers of high K^2 seasonal variability in the SWT, SEV and NEN regions

where pronounced seasonal cycles of K^1 are found. The consistency between the evolutions of K^1 and K^2 in Fig. 11 indicates that high-frequency synoptic eddies may participate in the seasonal modulation of mesoscale eddies.

To figure out how the synoptic eddies influence the mesoscale eddies, we show the annual cycles of the depth-integrated $\Gamma_A^{2\rightarrow 1}$ and $\Gamma_K^{2\rightarrow 1}$ averaged over the SCS and the three subdomains in Fig. 12. The negative $\Gamma_A^{2\rightarrow 1}$ and $\Gamma_K^{2\rightarrow 1}$ indicate that both APE and KE are transferred downscale from the mesoscale to the synoptic eddies in the SCS, in agreement with recent studies (e.g., Zhang et al., 2016). In other words, the synoptic eddies serve as a sink of mesoscale eddy energy and act to damp the mesoscale eddies. A closer look at the results in Fig. 12 reveals that the canonical transfers between the mesoscale and the synoptic windows exhibit seasonal cycles roughly out of phase with that of mesoscale EKE. Both $\Gamma_A^{2\rightarrow 1}$ and $\Gamma_K^{2\rightarrow 1}$ reach minima in winter, autumn and winter in the SWT, SEV and NEN regions, respectively, corresponding to the K^1 peaks in the same seasons in the respective regions. The negative correlations between K^1 and the mesoscale-synoptic canonical transfers imply that the small-scale eddies do not play a part in the seasonal variation of the SCS mesoscale eddies. This is different from the situation in other ocean sectors such as the North Pacific Subtropical Countercurrent where small-scale eddies are found to modulate the mesoscale EKE via inverse cascade process (Qiu et al., 2014). Furthermore, we notice that in the regions of SWT and SEV the amplitude of $\Gamma_K^{2\rightarrow 1}$ is larger than that of $\Gamma_A^{2\rightarrow 1}$ (Fig. 12b–c), implying that the mechanical energy transferred across the two scale windows are mainly in the form of KE. It should be noted that compared with the interaction between background flow and mesoscale eddies (i.e., the baroclinic and barotropic instabilities described in section 4.2), the mesoscale-synoptic interaction is almost one order smaller in magnitude, thus it is insufficient to significantly affect the annual cycles of the mesoscale EKE.

4.4. Mesoscale eddy wind work

As a predominant trigger for the SCS circulation, wind forcing has been considered to induce mesoscale eddies in the SCS (e.g., Wang et al., 2003; Zhang et al., 2019). To examine the direct action of wind on the
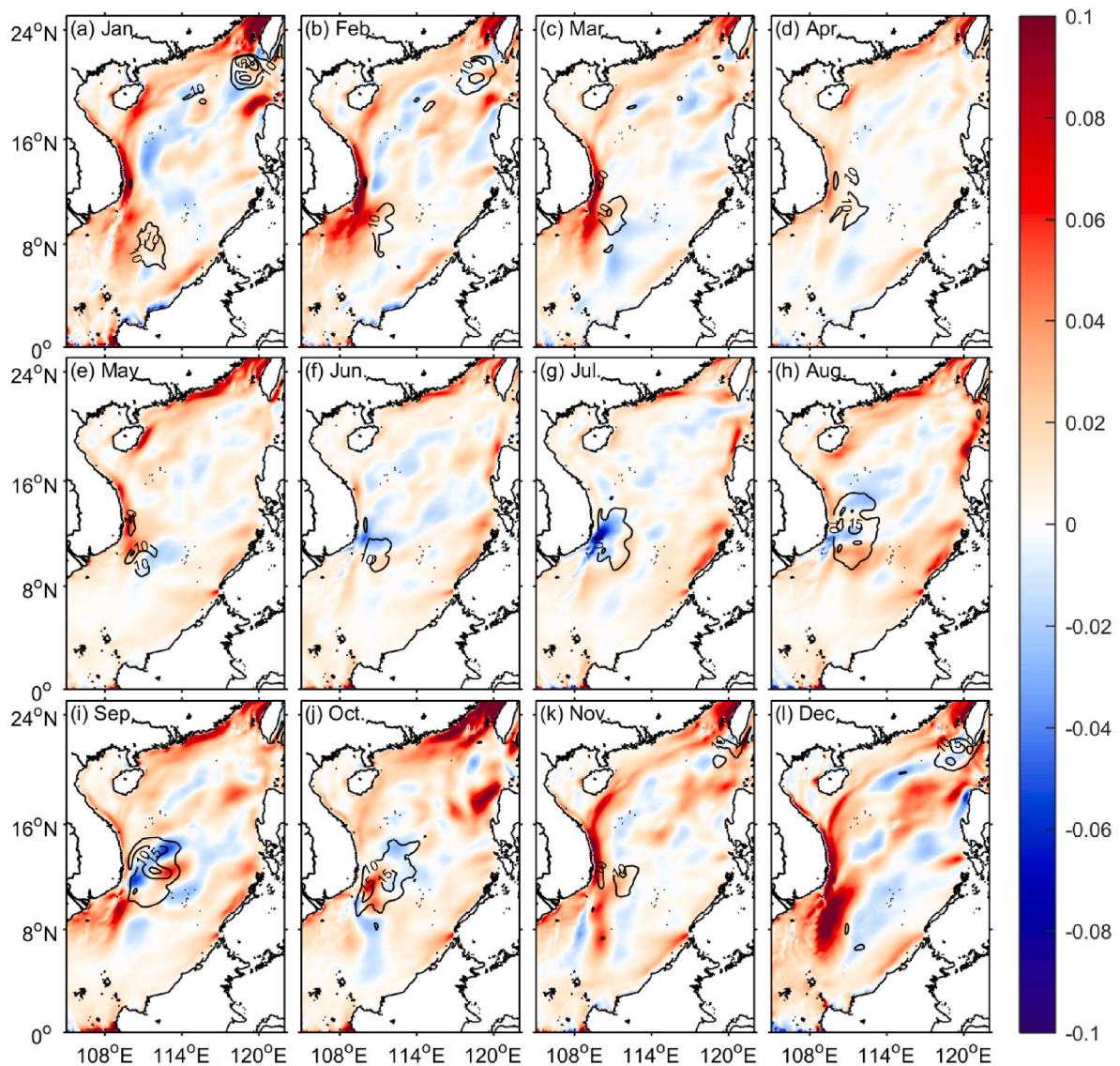
Fig. 13. Climatological monthly maps of mesoscale EWW (shadings; cm^3/s^3). The depth-integrated K^1 (contours; m^3/s^2) equal to or larger than 10 m^3/ s^2 is contoured.

oceanic mesoscale eddies in the SCS, we estimate the eddy wind work (EWW) on the mesoscale window by Eqn. (4) using the datasets from HYCOM and CFSR. Fig. 13 displays the climatological spatial distributions of EWW month by month. Positive (negative) value means that the mesoscale eddies gain (lose) KE from (to) the atmospheric wind. It is found that the local wind is likely to impact the seasonal modulation of mesoscale eddies in the NEN region, but not in the SWT and SEV regions. Fig. 13 shows that in winter when K^1 in the NEN region is enhanced, the domain is dominated by strong positive EWW, indicating that strong energy is directly fed to mesoscale eddies from the local wind during this time; in other seasons when K^1 is decreased, the NEN region is observed to show weak signals of EWW. In contrast, EWW in the SWT and SEV regions show low correlations with mesoscale EKE. For example, in some high-K^1 months such as December in SWT and July in SEV, the K^1 centers are occupied by negative EWW, indicative of a damping role played by the local wind. Also, in some low-K^1 months such as October in SWT and February in SEV, the regions are dominated by positive EWW. The disagreement between seasonal phases of EWW and K^1 suggest that the local wind is not the controlling factor on the mesoscale eddy seasonality in the SWT and SEV regions.

To clearly show the relationship between the mesoscale EKE and

EWW, we also plot the annual cycles of averaged EWW in Fig. 10 (green lines). When averaged throughout the whole SCS (Fig. 10a), the EWW annual cycle seems to have a close correlation with the K^1 annual cycle, indicating that the wind is related to the seasonal K^1 modulation from a basin scale perspective. When the three subregions are considered separately, it is found that EWW is responsible for the seasonal K^1 variation only in the NEN region. Fig. 10d shows that EWW in the NEN region is highly correlated with that of K^1, with the correlation coefficient reaching 0.8. The EWW done to mesoscale eddies is maximized in winter, corresponding to the K^1 peak in the same season in this region. It is noted that the amplitude of the EWW annual cycle in the NEN region is in the same magnitude with that of $\Gamma_K^{0 \to 1}$, indicating that the local wind and the barotropic instability of the background flow are both important to the seasonal variability of mesoscale eddies in this region. The scenarios are quite different in the SWT and SEV regions. Fig. 10b–c reveal that the annual cycles of EWW and K^1 are out of phase in these regions. The peak of EWW in the SWT region leads the K^1 peak by 3 months; the annual cycle of EWW in the SEV region is roughly out of phase with that of K^1. These results indicate that local wind plays an important role in modulating the seasonal variability of mesoscale EKE in the NEN region, while it does not participate directly in the seasonal modulation in the

SWT and SEV regions.

5. Conclusions

In this study, we employ a recently developed tool, multiscale window transform (MWT), and the MWT-based theory of canonical transfer to investigate the dynamical processes related to the seasonal eddy variability in the SCS. Using MWT, the original fields are decomposed into subfields on a nonstationary background flow window (periods >256 days), a mesoscale window (periods of 32–256 days) and a high-frequency synoptic window (periods <32 days). Based on the $1/12.5°$ HYCOM reanalysis data, the instabilities and the nonlinear scale interactions are quantified in terms of canonical transfer, which has a Lie bracket form and conserves energy through scales. Three local regions of high mesoscale EKE levels, i.e., the southwest of Taiwan Island (SWT), the southeast of Vietnam (SEV) and the northeast of the Natuna Island (NEN), are considered in this study. It is found that the seasonal cycles of the mesoscale EKE are not in phase in the three regions, with peaks occurring in January, October and December, respectively.

By diagnosing the canonical transfers between the background flow window and the mesoscale window, the relative contributions from baroclinic and barotropic instabilities to the seasonal mesoscale eddy variability in the three considered subdomains are quantified. In the SWT region, the strengths of the barotropic and baroclinic instabilities are comparable, and both processes are in phase with the local mesoscale EKE, implying a mixed instability mechanism for the eddy generation in this region. In contrast, barotropic instability plays a dominant role in determining the EKE seasonality in the SEV and NEN regions, while the seasonal cycles of the baroclinic instabilities in these two regions are substantially weaker than those of their barotropic counterparts. The seasonal cycle of the barotropic instability processes is found to be closely related with the strength of the mean flow in all the three considered regions.

The three-scale energetics framework further reveals that energy cascade between the mesoscale and synoptic windows is generally in a forward sense and the strength of the forward cascade is significantly enhanced when the mesoscale eddy activities are strong. This indicates that the high-frequency synoptic motions in the SCS generally serve as an energy sink for the mesoscale eddies, consistent with previous studies based on *in situ* observations.

The seasonal variability of the wind work done to the mesoscale eddies is also examined. Our result shows that the eddy wind work (EWW) is not in phase with the mesoscale EKE in the SWT and SEV regions, suggesting that internal instability is the primary generation mechanism in these two regions. In contrast, the EWW is well correlated with the EKE in the NEN region and has a comparable amplitude with the barotropic instability, indicating that both external wind forcing and internal process are responsible for the seasonal eddy variability in this region.

It should be noted that this study only focuses on the multiscale interaction and wind work processes that are related to the generation of the mesoscale eddy energy in the SCS. These processes must be balanced by other processes such as the nonlocal energy advection, pressure work and internal dissipations in the energy budget equations [Eqs. (5) and (6)]. Investigations of the complete energy cycle and its associated temporal variation are more suitable using free-run models since the physical fields from reanalysis products (e.g., HYCOM reanalysis) are not dynamically consistent. We will henceforth set up a model and give these a detailed a study.

Declaration of competing interest

The authors declare that they have no known competing financial interests or personal relationships that could have appeared to influence the work reported in this paper.

References

Cai, S., Long, X., Wang, S., 2007. A model study of the summer southeast Vietnam offshore current in the southern South China sea. Continent. Shelf Res. 27 (18), 2357–2372. https://doi.org/10.1016/j.csr.2007.06.002.

Chelton, D.B., Schlax, M.G., Samelson, R.M., 2011. Global observations of nonlinear mesoscale eddies. Prog. Oceanogr. 91 (2), 167–216. https://doi.org/10.1016/j. pocean.2011.01.002.

Chen, G., Gan, J., Xie, Q., Chu, X., Wang, D., Hou, Y., 2012. Eddy heat and salt transports in the South China Sea and their seasonal modulations: eddy transports in the SCS. J. Geophys. Res.: Oceans 117 (C5). https://doi.org/10.1029/2011JC007724 n/a-n/ a.

Chen, G., Hou, Y., Zhang, Q., Chu, X., 2010. The eddy pair off eastern Vietnam: interannual variability and impact on thermohaline structure. Continent. Shelf Res. 30 (7), 715–723. https://doi.org/10.1016/j.csr.2009.11.013.

Cheng, X., Qi, Y., 2010. Variations of eddy kinetic energy in the South China Sea. J. Oceanogr. 66 (1), 85–94. https://doi.org/10.1007/s10872-010-0007-y.

Cummings, J.A., 2005. Operational multivariate ocean data assimilation. Q. J. R. Meteorol. Soc. 131 (613), 3583–3604. https://doi.org/10.1256/qj.05.105.

Cummings, J.A., Smedstad, O.M., 2013. Variational data assimilation for the global ocean. In: Park, S.K., Xu, L. (Eds.), Data Assimilation for Atmospheric, Oceanic and Hydrologic Applications, vol. II. Springer Berlin Heidelberg, Berlin, Heidelberg, pp. 303–343. https://doi.org/10.1007/978-3-642-35088-7_13.

Ferrari, R., Wunsch, C., 2009. Ocean circulation kinetic energy: reservoirs, sources, and sinks. Annu. Rev. Fluid Mech. 41 (1), 253–282. https://doi.org/10.1146/annurev. fluid.40.111406.102139.

Gan, J., Li, H., Curchitser, E.N., Haidvogel, D.B., 2006. Modeling South China Sea circulation: response to seasonal forcing regimes. Journal of Geophysical Research Oceans 111 (C6). https://doi.org/10.1029/2005JC003298.

Gan, J., Qu, T., 2008. Coastal jet separation and associated flow variability in the southwest South China sea. Deep Sea Res. Oceanogr. Res. Pap. 55 (1), 1–19. https:// doi.org/10.1016/j.dsr.2007.09.008.

Hu, J., Kawamura, H., Hong, H., Qi, Y., 2000. A review on the currents in the south China sea: seasonal circulation, South China sea warm current and Kuroshio intrusion. J. Oceanogr. 56 (6), 607–624. https://doi.org/10.1023/a:1011117531252.

Hwang, C., Chen, S.-A., 2000. Circulations and eddies over the South China Sea derived from TOPEX/Poseidon altimetry. Journal of Geophysical Research Oceans 105 (C10), 23943–23965.

Jouanno, J., Sheinbaum, J., Barnier, B., Molines, J.M., Candela, J., 2012. Seasonal and interannual modulation of the eddy kinetic energy in the Caribbean Sea. J. Phys. Oceanogr. 42 (11), 2041–2055. https://doi.org/10.1175/JPO-D-12-048.1.

Kang, D., Curchitser, E.N., Rosati, A., 2016. Seasonal variability of the Gulf Stream kinetic energy. J. Phys. Oceanogr. 46 (4) https://doi.org/10.1175/JPO-D-15-0235.1, 160224111526006.

Li, Q., Zhou, L., Xie, L., 2021. Seasonal and interannual variability of EAPE in the south China sea derived from ECCO2 data from 1997 to 2019. Water 13 (7), 926. https:// doi.org/10.3390/w13070926.

Liang, X.S., 2016. Canonical transfer and multiscale energetics for primitive and quasigeostrophic atmospheres. J. Atmos. Sci. 73 (11), 4439–4468. https://doi.org/ 10.1175/JAS-D-16-0131.1.

Liang, X.S., Anderson, D.G.M., 2007. Multiscale window transform. Multiscale Model. Simul. 6 (2), 437–467. https://doi.org/10.1137/06066895X.

Liang, X.S., Robinson, A.R., 2007. Localized multi-scale energy and vorticity analysis. Dynam. Atmos. Oceans 44 (2), 51–76. https://doi.org/10.1016/j. dynatmoce.2007.04.001.

Nan, F., Xue, H., Yu, F., 2015. Kuroshio intrusion into the south China sea: a review. Prog. Oceanogr. 137, 314–333. https://doi.org/10.1016/j.pocean.2014.05.012. SEP.PT.A.

Pedlosky, J., 1979. Geophysical Fluid Dynamics. Springer-Verlag, p. 624.

Qiu, B., Chen, S., Klein, P., Sasaki, H., Sasai, Y., 2014. Seasonal mesoscale and submesoscale eddy variability along the north pacific subtropical countercurrent. J. Phys. Oceanogr. 44 (12), 3079. https://doi.org/10.1175/JPO-D-14-0071.1.

Quan, Q., Cai, Z., Jin, G., Liu, Z., 2021. Topographic rossby waves in the abyssal South China sea. J. Phys. Oceanogr. 51 (6), 1795–1812. https://doi.org/10.1175/JPO-D-20-0187.1.

Sérazin, G., Penduff, T., Barnier, B., Molines, J.-M., Arbic, B.K., Müller, M., Terray, L., 2018. Inverse cascades of kinetic energy as a source of intrinsic variability: a global OGCM study. J. Phys. Oceanogr. 48 (6), 1385–1408. https://doi.org/10.1175/JPO-D-17-0136.1.

Storch, J.-S. von, Eden, C., Fast, I., Haak, H., Hernández-Deckers, D., Maier-Reimer, E., Stammer, D., 2012. An estimate of the lorenz energy cycle for the world ocean based on the STORM/NCEP simulation. J. Phys. Oceanogr. 42 (12), 2185–2205. https://doi.org/10.1175/JPO-D-12-079.1.

Von Storch, J.-S., Eden, C., Fast, I., Haak, H., Hernández-Deckers, D., Maier-Reimer, E., et al., 2012. An estimate of the lorenz energy cycle for the world ocean based on the STORM/NCEP simulation. J. Phys. Oceanogr. 42 (12), 2185–2205. https://doi.org/10.1175/JPO-D-12-079.1.

Wang, D., Liu, Q., Xie, Q., He, Z., Zhuang, W., Shu, Y., et al., 2013. Progress of regional oceanography study associated with western boundary current in the South China Sea. Chin. Sci. Bull. 58 (11), 1205–1215. https://doi.org/10.1007/s11434-012-5663-4.

Wang, G., Chen, D., Su, J., 2006. Generation and life cycle of the dipole in the South China Sea summer circulation. J. Geophys. Res. 111 (C6), C06002. https://doi.org/10.1029/2005JC003314.

Wang, G., Su, J., Chu, P.C., 2003. Mesoscale eddies in the South China Sea observed with altimeter data. Geophys. Res. Lett. 30 (21), 2121. https://doi.org/10.1029/2003GL018532.

Wang, H., Wang, D., Liu, G., Wu, H., Li, M., 2012. Seasonal variation of eddy kinetic energy in the South China Sea. Acta Oceanol. Sin. 31 (1), 1–15. https://doi.org/10.1007/s13131-012-0170-7.

Wyrtki, K., 1961. Physical oceanography of the southeast Asian waters, Scientific results of marine investigations of the South China Sea and the Gulf of Thailand. NAGA Rep 2, 195 (Scripps Inst. of Oceanogr., La Jolla, Calif).

Xie, L., Zheng, Q., Zhang, S., Hu, J., Li, M., Li, J., Xu, Y., 2018. The Rossby normal modes in the South China Sea deep basin evidenced by satellite altimetry. Int. J. Rem. Sens. 39 (1–2), 399–417. https://doi.org/10.1080/01431161.2017.1384591.

Xiu, P., Chai, F., Shi, L., Xue, H., Chao, Y., 2010. A census of eddy activities in the South China Sea during 1993–2007. J. Geophys. Res. 115 (C3), C03012. https://doi.org/10.1029/2009JC005657.

Xue, H., Chai, F., Pettigrew, N., Xu, D., Shi, M., Xu, J., 2004. Kuroshio intrusion and the circulation in the south China sea. Journal of Geophysical Research Oceans 109 (C2). https://doi.org/10.1029/2002JC001724.

Yang, Haijun, Liu, Q., Liu, Z., Wang, D., Liu, X., 2002. A general circulation model study of the dynamics of the upper ocean circulation of the South China Sea. J. Geophys. Res. 107 (C7), 3085. https://doi.org/10.1029/2001JC001084.

Yang, Haiyuan, Wu, L., Liu, H., Yu, Y., 2013. Eddy energy sources and sinks in the South China Sea. Journal of Geophysical Research Oceans 118 (9), 4716–4726. https://doi.org/10.1002/jgrc.20343.

Yang, Y., Liang, X.S., 2018. On the seasonal eddy variability in the Kuroshio extension. J. Phys. Oceanogr. 48 (8), 1675–1689. https://doi.org/10.1175/JPO-D-18-0058.1.

Yang, Y., Liang, X.S., 2019. New perspectives on the generation and maintenance of the Kuroshio large meander. J. Phys. Oceanogr. 49 (8), 2095–2113. https://doi.org/10.1175/JPO-D-18-0276.1.

Zhang, M., von Storch, H., Chen, X., Wang, D., Li, D., 2019. Temporal and spatial statistics of travelling eddy variability in the South China Sea. Ocean Dynam. https://doi.org/10.1007/s10236-019-01282-2.

Zhang, Z., Tian, J., Qiu, B., Zhao, W., Chang, P., Wu, D., Wan, X., 2016. Observed 3D structure, generation, and dissipation of oceanic mesoscale eddies in the south China sea. Sci. Rep. 6 (1) https://doi.org/10.1038/srep24349.

Zhang, Z., Zhao, W., Qiu, B., Tian, J., 2017. Anticyclonic eddy sheddings from Kuroshio loop and the accompanying cyclonic eddy in the northeastern South China sea. J. Phys. Oceanogr. 47 (6), 1243–1259. https://doi.org/10.1175/JPO-D-16-0185.1.

Zhao, Y.-B., Liang, X.S., Gan, J., 2016. Nonlinear multiscale interactions and internal dynamics underlying a typical eddy-shedding event at Luzon Strait: luzon eddy-shedding dynamics. J. Geophys. Res.: Oceans 121 (11), 8208–8229. https://doi.org/10.1002/2016JC012483.